Physics of the Earth and Planetary Interiors 287 (2019) 51–64

Contents lists available at ScienceDirect

Physics of the Earth and Planetary Interiors

journal homepage: www.elsevier.com/locate/pepi

Lithospheric seismic structure beneath two broadband station sites of the eastern part of Chhotanagpur Plateau: New constraints from receiver functions and dispersion curves

Mukesh Kumar Das[a], Mohit Agrawal[a,*], Ravindra K. Gupta[a], J.L. Gautam[b]

[a] Indian Institute of Technology (Indian School of Mines), Dhanbad, India
[b] National Center for Seismology, Ministry of Earth Sciences, Govt. of India, India

ARTICLE INFO

Keywords:
Receiver functions
Dispersion curves
Chhotanagpur Plateau
Crustal thickening
Uncertainty analysis
Very fast simulated annealing

ABSTRACT

The Chhotanagpur Plateau in eastern India was formed due to the severe upheaval of tectonic forces deep inside the earth. The deep geological processes associated with its subsurface along with geodynamical rationales are never understood properly due to the dearth of good quality geophysical data. We use high quality teleseismic earthquakes' waveforms ($5.5 \leq M \leq 8.0$) recorded at two seismic stations ISM and BOKR located in Dhanbad and Bokaro, respectively. These data are used to jointly model discrete but complementary datasets such as Ps and Sp receiver functions and Rayleigh wave group velocity dispersion curves via Very Fast Simulated Annealing (VFSA). A two-step optimization procedure is carried out to find the best fitting models and associated uncertainties in terms of Posterior Probability Density (PPD) functions. Our results reveal that on an average the eastern part of Chhotanagpur plateau which is mostly composed of Granite Gneiss Complex with high heat flow is characterized by the thick crust. For ISM station up to ~150 km depth, Vp and Vs vary between 6.1 km/s–8.4 km/s and 3.3 km/s–4.8 km/s, respectively. We observe that Vp and Vs ranges between ~6.2 km/s to ~8.3 km/s and ~3.2 km/s to ~4.6 km/s, respectively, for seismic station BOKR. We find that the crustal thickness beneath seismic stations ISM and BOKR is ~43 and ~44 km, respectively. The higher values of Poisson's ratio (> 0.25) for station ISM and BOKR are 0.30 and 0.29, respectively which may indicate the presence of partial melt present in the lower crust.

1. Introduction

The Indian Shield is made up of tectonically complex framework during long history ranging from Archean to Cenozoic (Ratheesh Kumar et al., 2013). It is complex because it is formed from assemblages of the diverse set of tectonic features with varying age, lithology, composition, geothermal gradient etc. In general, the Indian Shield with a ~3 billion years old tectonic history, is a collage of mainly five Archean age cratonic nuclei viz., Singhbhum, Aravali, Bundelkhand, Dharwar, and Bastar. It also consists of three plateaus namely Malwa Plateau, Deccan Plateau and Chhotanagpur Plateau (Naqvi and Rogers, 1987; Meert et al., 2010). Among all these cratons and plateaus, Chhotanagpur Plateau's lithospheric seismic structure is least understood due to the deficiency of adequate data without any common consensus (Figs. 1a and 1b). Chhotanagpur Plateau is majorly characterized by Chhotanagpur Granite Gneiss Complex (CGGC), which is an integral part of the Stable Continental Peninsular Region (SCPR) of Indian shield (Ghose et al., 2008). The depth estimates of Moho discontinuity, a layer between crust and mantle which is mostly characterized by abrupt changes in seismic P-and S-wave velocities, along Chhotanagpur Plateau have been produced using few geophysical techniques such as surface wave dispersion, Bouguer gravity anomaly, Ps receiver functions and magnetotelluric study (Qureshy, 1971; Bhattacharya, 1971; Kumar et al., 2001; Bhattacharya and Shalivahan, 2002; Sharma et al., 2014). However, the results of these researches are constrained either by the dearth of data coverage or moderate to low data quality.

To enhance the earthquake detection capability of the eastern part of the Chhotanagpur Plateau (EPCP) and to better understand the geodynamical rationales responsible for the thickening and dehydration of EPCP (Kumar et al., 2001; Bhattacharya and Shalivahan, 2002); two broadband seismic stations were set up during the years 1993 (upgraded to the standards of Global Seismic Networks (GSN) in 1997) and 1999 in the campus premises of Indian Institute of Technology (Indian School of Mines), Dhanbad (IIT(ISM)) and Bokaro Steel City;

* Corresponding author.
E-mail address: mohit@iitism.ac.in (M. Agrawal).

https://doi.org/10.1016/j.pepi.2019.01.004
Received 13 September 2018; Received in revised form 7 January 2019; Accepted 8 January 2019
Available online 09 January 2019
0031-9201/

Fig. 1a. Tectonic set up of Indian shield shows the major Cratons, Plateaus, Basins and Garbens etc. The red box represents the study area which we have further explained with details tectonic features in Fig. 1(b). (For interpretation of the references to color in this figure legend, the reader is referred to the web version of this article.)

respectively. A CMG-40T Digital Seismograph connected to a DM24 data acquisition system is functioning at IIT(ISM), which is having a sampling rate of 100 samples/s with amplification factor of 1.0. This seismograph has been placed over an aboriginal 13′ long concrete seismic pillar within the geodetic observatory at IIT(ISM). This observatory is located at latitude and longitude of 23.82° N and 86.44° E with elevation of 227 m from mean sea level (M.S.L.). The seismic station in Bokaro is equipped with STS-2 broadband sensor which is situated at 23.78° N and 85.88° E with M.S.L. of 210 m. One attempt has been made for finding the crustal seismic structure at Bokaro's broadband seismic station (with station code BOKR) using Ps receiver functions computed from limited amount of earthquake data. But, it could not resolve the depth of crust-mantle boundary owing to complexity in seismological data (Kumar et al., 2001). From H-κ stacking of Ps receiver functions, the Moho depth was found to be at ~42.2 km and bulk Vp/Vs ratio of ~1.92 beneath the ISM's broadband seismic station (Sharma et al., 2014). But this study failed to provide an estimate of depth variations of P-and S-wave velocities in the crust and upper mantle.

To address these intriguing issues, we investigate P-and S-wave velocity structure of EPCP by jointly modeling Ps and Sp receiver functions and Rayleigh wave group velocity dispersion curves computed from relatively large amount of earthquake data acquired at ISM and BOKR, using global nonlinear optimization technique such as Very Fast Simulated Annealing (VFSA). Ps receiver functions are more useful in constraining the sharp S-wave velocity contrast in the crust; while Sp receiver functions are more sensitive to the abrupt changes in S-wave velocities in the lithospheric mantle (due to its larger wavelength) (Ammon et al., 1990). The Rayleigh wave group velocity dispersion curves put larger constraints on the averages of absolute S-wave velocities (Tanimoto, 1991). So, the joint modeling will merge the information from these individual datasets into a single modeling scheme by complementing each other and will provide better and more reliable estimates of seismic P-and S-wave velocities (Ozalaybey et al., 1997; Agrawal et al., 2015a,b; Kumar and Agrawal, 2018). To begin the joint modeling process, an Initial crustal model is set up based on the Moho depth and bulk Vp/Vs ratios obtained from the H-κ stacking method (Zhu and Kanamori, 2000). Reliability of the final best fitting models is assessed by using Posterior Probability Density functions (PPDs). This statistical tool allows us to identify those portions of the final best fitting models that are well or less constrained (Gangopadhyay et al., 2007; Agrawal et al., 2015a,b; Kumar and Agrawal, 2018).

2. Tectonic setting

The Chhotanagpur Plateau, which has areal extent approximately

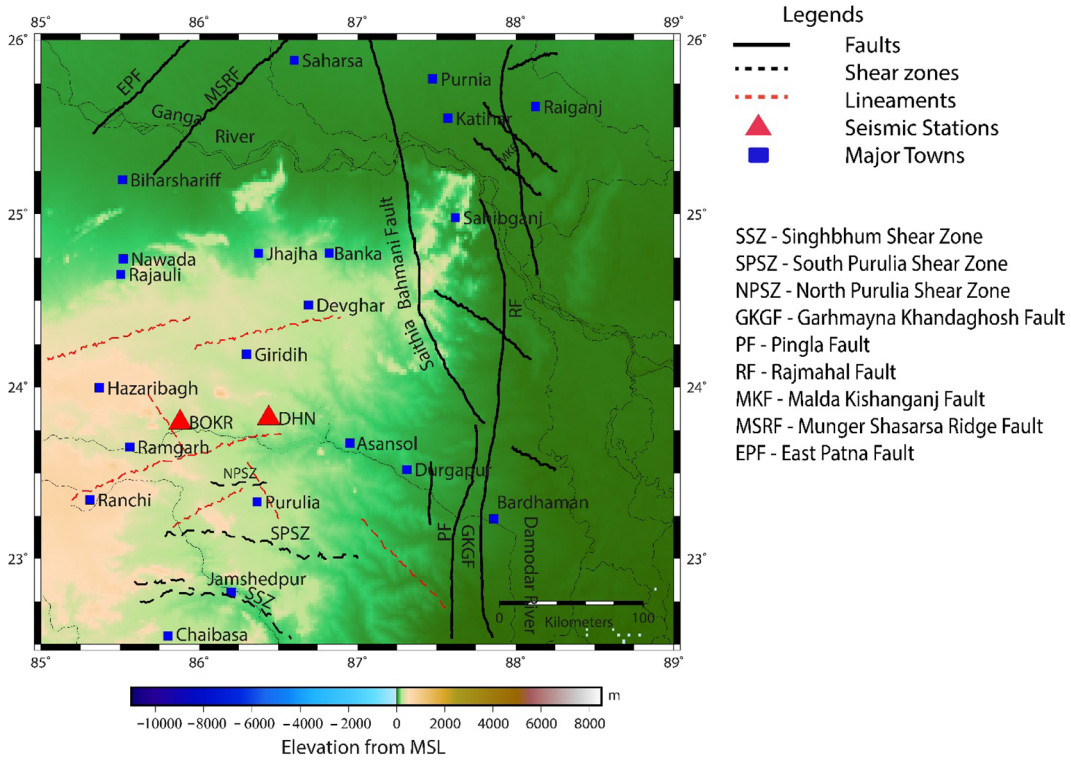

Fig. 1b. Tectonic map of East Indian Shield modified from Sharma et al. (2014); some important geological features in this area are Singhbhum Shear Zone (SSZ), South Purulia Shear Zone (SPSZ), North Purulia Shear Zone (NPSZ), Garhmayana Khandaghosh Fault (GKGF), Pingla Fault (PF), Rajmahal Fault (RF), Malda Kishanganj Fault (MKF), Munger Shasarsa Ridge Fault (MSRF) and East Patna Fault (EPF). Location of broadband seismograph stations are shown by red triangles and the blue boxes represent major towns nearby our study area. (For interpretation of the references to color in this figure legend, the reader is referred to the web version of this article.)

up to 65,000 square kilometers (or 25,000 square miles), is located in East Indian states of Jharkhand, Odisha, West Bengal, Bihar, and Chhattisgarh. Although, a significant part of the Chhotanagpur Plateau lies in Jharkhand which is surrounded by Indo-Gangetic plain in the north and east, and the Mahanadi River basin in the south. It is a continental plateau formed from the continental upheaval of tectonic forces deep inside the earth during the Cretaceous. The adjacent areas of Chhotanagpur plateau host various regional faults, i.e., Singhbhum Shear Zone, Saharsa Ridge Fault, and East Patna Fault etc. The faults are orthogonally transecting the Himalayan Frontal Thrust (Fig. 1b) (Sharma et al., 2014). The plateau's primeval origin can be demonstrated from Gondwana substrates, a part of Deccan Plate, which it took almost 50-million-years to set itself free from the southern continent which was fiercely disrupted by northern Eurasian continent (Mukhopadhyay et al., 2008).

The EPCP can majorly be classified into two main geographical regions, first lies in southern part covered by the Ranchi plateau, the Singhbhum region, and the Patland region and the second lies in the northern part that consists of Santhal Pargana uplands, Hazaribag-Damodar Valley and Palamau Uplands. The Ranchi plateau is the largest block of Chhotanagpur plateau with an average elevation of 700 m; which gradually slopes down towards south-east into the hilly and undulating region of Singhbhum craton (Singh, 1997). In the north, the Ranchi plateau is separated from Hazaribagh Plateau by Damodar trough, and, Patlands are situated to its west which has an average elevation of 1000 m above mean sea level (Mahadevan, 2002). Hazaribag Plateau can be subdivided into two sections: lower plateau and higher plateau; which are commonly referred as Koderma Plateau and Hazaribag Plateau, respectively. In the northeastern and southern faces, the Hazaribagh plateau is connected to Ranchi plateau through Tori Pargana. The eastern part of the Koderma plateau is sloping down gently and uniformly which is continuing past the Barakar River. The Barakar River traverses Giridih and Koderma districts in the easterly direction.

3. Methodology

The methodology that we follow for jointly model Ps, Sp receiver functions and Rayleigh wave group velocity dispersion curve has been shown in the flow diagram (Fig. 2). All the steps are described below:

Step 1: Ps and Sp receiver function's and Rayleigh wave group velocity estimation

Receiver functions are spike-like wave trains in time domain consisting of converted body waves and are sensitive to subsurface structure near the receiver. Receiver functions can be classified into two types, namely, Ps receiver functions and Sp receiver functions. Ps receiver functions (also referred as 'Radial Receiver Functions') are estimated by deconvolving the vertical component from the radial component and hence represents a scaled version of the radial component with P-wave reverberations removed (Langston, 1979). In contrast to Ps receiver functions, the Sp receiver functions (also referred as 'Vertical Receiver Functions') are computed by deconvolving radial component seismograms from vertical component seismograms. The Sp receiver functions provide additional advantages as compared to Ps receiver functions because they are free from shallow layers' multiples in the time window of Sp converted phases (Kumar et al., 2005). The Ps and Sp receiver function's amplitude and arrival times of the converted waves are sensitive to P-and S-wave velocities (for fixed layer thicknesses) and density in the crust and lithospheric mantle (Owens et al., 1984).

For receiver function's generation, the earthquake waveforms are recorded for years 2007–2017 and 2008–2015 for seismic stations ISM

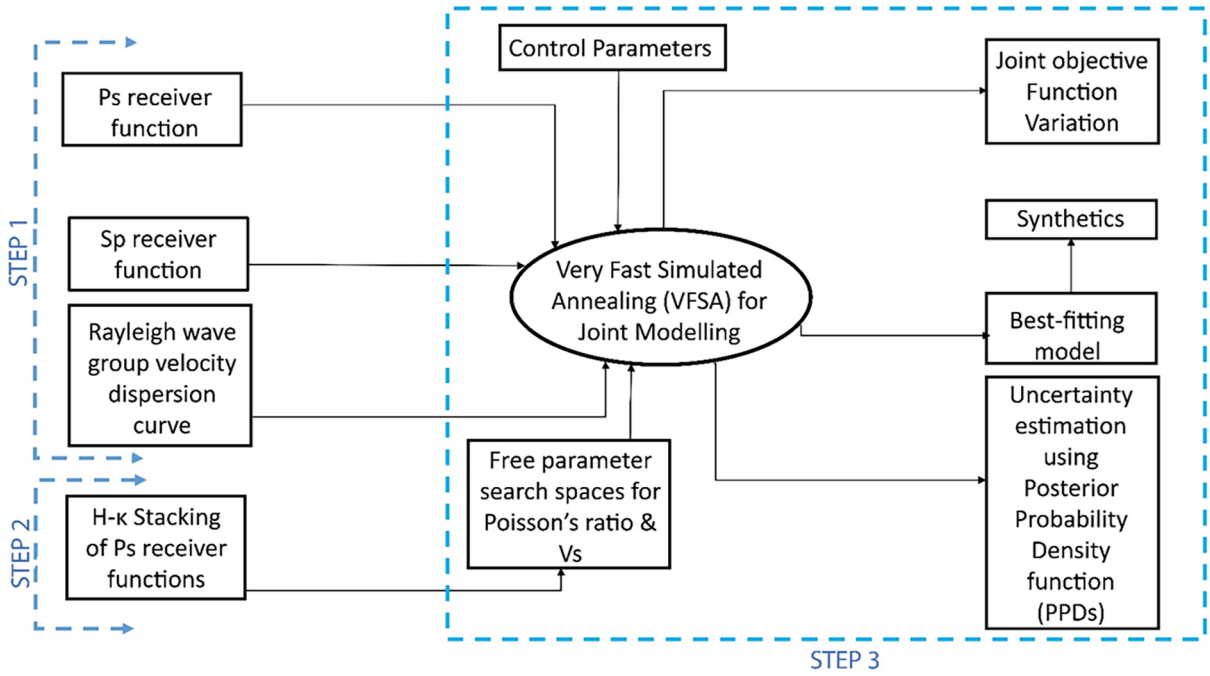

Fig. 2. Schematic flow diagram depicting the major steps considered for joint modeling of Ps and Sp receiver functions and Rayleigh wave group velocity dispersion curves. We adopt a three steps procedure for finding major geological features beneath the eastern part of Chhotanagpur plateau.

and BOKR, respectively. An earthquakes' distribution w.r.t. their epicenter locations along with histogram showing the number of earthquakes with backazimuths are shown in Fig. 3a and b, respectively. We manually pick P-and S-wave arrivals on each seismogram. All waveforms are visually inspected for quality control. Finally, 693 and 619 teleseismic earthquake events ($5.5 \leq M \leq 8.0$) are selected for receiver functions' calculations. Then, events with epicentral distance range of 30°–95° and 60°–95° are utilized for the generation of Ps and Sp receiver functions. For Ps and Sp receiver function's computation, seismograms are rotated to radial and transverse components using event's backazimuth. Particularly for Ps receiver functions, we extract 35 s of recording by cutting the seismogram 5 s before and 30 s after the P-wave arrival. For Sp receiver functions, earthquake waveforms are windowed 30 s before and 5 s after the S-wave arrival. Next, all the preprocessed seismograms are detrended, tapered, and decimated to a uniform sample rate of 20 samples per seconds. The Ps and Sp receiver functions are estimated using an iterative time domain deconvolution technique with 200 iterations (Ligorria and Ammon, 1999). This deconvolution technique controls the frequency content of receiver functions by Gaussian width parameter 'a'. For finding gross subsurface geological features, two Gaussian width parameter, $a = 2.0$ (< 0.75 Hz) and $a = 2.5$ (< 1.25 Hz), are considered for calculating Sp and Ps receiver functions, respectively. Only those receiver functions are considered for further analysis for which deconvolution produces more than 90% of signal energy. Finally, we obtain a total of 191 Ps receiver functions for seismic station ISM with backazimuths and rayparameters ranging from 22° to 349° and 0.0415 to 0.080, respectively (Fig. 4a and b). A total of 17 Sp receiver functions are computed for ISM with backazimuths and rayparameters varying from 36° to 349° and 0.084 to 0.119, respectively (Fig. 4c and d). For BOKR, we use a total of 164 Ps receiver functions with backazimuths and rayparameters lying between 3°–350° and 0.044–0.080, respectively (Fig. 5a and b). While, 18 Sp receiver functions are calculated with backazimuth range 36°–119° and ray parameter range 0.084–0.124 (Fig. 5c and d).

The individual envelop of each seismic surface wave travels at a different speed such that individual harmonic component appears distinctly. Although, dispersion curves can be classified into group and phase velocity, we use utilizing only group velocity dispersion curves because these are relatively easier to measure (information of source phase not need) and can be estimated for shorter periods in order to delineate shallower crustal acoustic properties. A dispersion curve is a graphical representation of group velocities versus period. The dispersion curves provide constraints to the absolute shear wave velocities but less sensitive to impedance contrasts at discontinuities (Julia et al., 2000).

In the presented research, we use Multiple Filter Analysis technique on both of the seismic stations (i.e. ISM and BOKR) which applies a narrow band-pass Gaussian filter to the individual vertical component over a diverse set of periods (Dziewonski et al., 1969; Herrmann, 1973). The maximum amplitude and its arrival time are picked at each period on the envelop function and corresponding group velocities are estimated using great circle arc distance.

Step 2: H-κ stacking of ps receiver functions

Using an incorrect starting seismic velocity model during joint modeling may produce an unreliable image of the subsurface, especially in the presence of heterogeneous lateral velocity variations. Hence, having the reliable knowledge of P-and S-wave velocities in the starting model may significantly benefit the iterative process of joint modeling via Very Fast Simulated Annealing (VFSA). So, we decide to use the H-κ stacking technique of Zhu and Kanamori (2000), for deducing the reliable values of average crustal thickness and bulk Vp/Vs ratios. These values of crustal thickness and Vp/Vs ratio are later utilized to constrain crustal elastic properties such as Vp and Vs in our starting model for joint analysis.

The most significant arrivals on Ps receiver functions are converted Ps arrivals from Moho or mid-crustal discontinuities (e.g. Conrad discontinuity) and its reverberations such as PpPs and PsPs + PpSs, respectively. The relative time arrivals of these converted phases w.r.t. to direct P-wave arrival are functions of discontinuity depth and average P-and S-wave velocities. We gather these Ps receiver functions of ISM and BOKR seismic stations for a range of ray parameters (Figs. 4b and 5b) to illuminate subsurface lateral velocity variations. In H-κ stacking

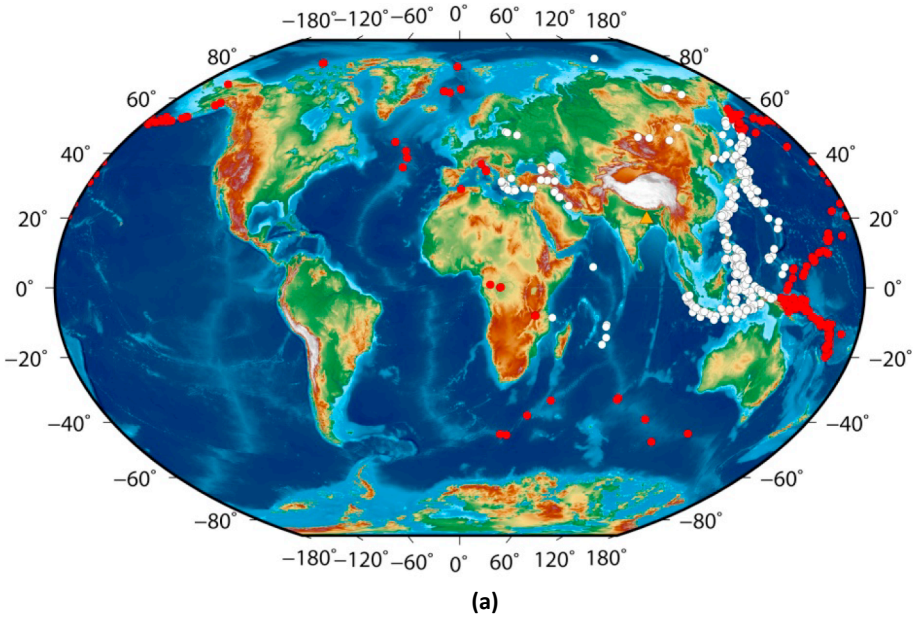

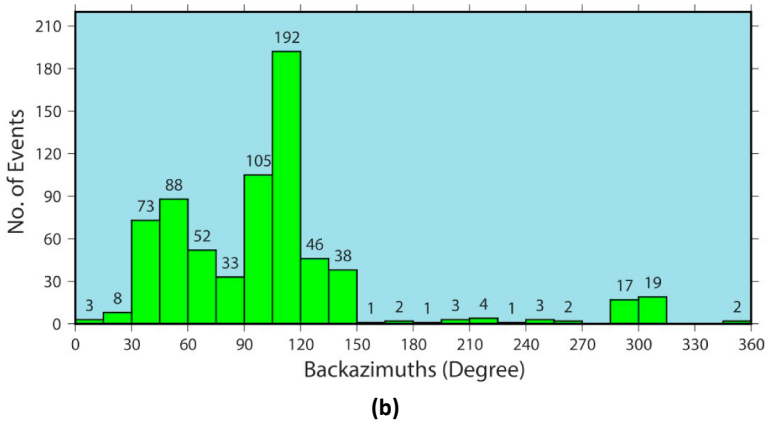

Fig. 3. (a) Teleseismic earthquake distribution for events occurred from years 2007 to 2017 for seismic stations ISM with magnitude (5.5 ≤ M ≤ 8.0). A total of 693 and 619 earthquake events are analysed for seismic stations ISM and BOKR. The white and red circles show earthquakes lying between epicentre distance range of 30°–60° (for Ps receiver functions) and 60°–95° (for Sp receiver functions). Orange color triangle represents the location of seismic stations. (b) Histogram of teleseismic earthquake events with their associated backazimuths for seismic stations BOKR and ISM recorded in between years 2007 and 2017. The significant seismicity is recorded between backazimuth range of 300–1500 with largest number (i.e. 192) of earthquake's energy arriving to both of the seismic stations (i.e. ISM and BOKR) in the backazimuth range of 105°–120° (i.e. 192). (For interpretation of the references to color in this figure legend, the reader is referred to the web version of this article.)

method, Ps receiver function's converted phases are stacked along their move out curves to estimate crustal thickness (H) and bulk Vp/Vs ratios (κ). This is grid search method where the arrival times of converted wave Ps and its reverberations PpPs and PsPs + PpSs are estimated based on predefined ranges of crustal thicknesses (H) and bulk Vp/Vs ratios (κ), for a given Vp. At each grid point (H, κ), the weighted sum of theses phase's amplitudes (i.e. w_1(Ps) = 0.6, w_2(PpPs) = 0.3, and w_3(PpSs + PsPs) = 0.1 (where, $\Sigma w_i = 1$) are maximized (i.e. max(S(H, κ))). The selection of weights is defined by the level of confidence through which these phases can be picked manually. The maximum value of S(H, κ) corresponds to the best values of average crustal thickness (H) and bulk Vp/Vs ratio (κ), where all three phases (i.e. Ps, PpPs and PsPs + PpSs) are stacked coherently. For H-κ stacking, we fix the Vp at 6.3 km/s similar to Zhu and Kanamori (2000); while H and κ are varied from 20 km to 60 km and 1.5 to 2.0, respectively, for both seismic stations i.e. ISM and BOKR. The best values of Moho depth and bulk Vp/Vs ratio are mapped at ~43 km and ~1.89 (Fig. 6a) for seismic station ISM. While at seismic station BOKR, we find the Moho at ~44 km depth and bulk Vp/Vs ratio of ~1.85 (Fig. 6b). With the help of these bulk Vp/Vs ratios, we can also calculate the Poisson's ratios for seismic stations ISM and BOKR using the following relation given below

$$\sigma = \frac{\left[1 - 2\left(\frac{Vs}{Vp}\right)^2\right]}{2\left[1 - \left(\frac{Vs}{Vp}\right)^2\right]} \quad (1)$$

where σ, Vp and Vs represent Poisson's ratio, shear wave and compressional wave velocities. The Poisson's ratios of ~0.30 and ~0.29 are obtained from Eq. (1) for seismic station ISM and BOKR, respectively.

Step 3: Joint modeling of mutually complementary datasets

Ps receiver functions have been jointly modeled with Rayleigh or Love wave's phase or group velocities and it has been established by several previous workers that jointly using these distinct and mutually complementary datasets have the ability to find more unique, reliable and realistic estimates of P-and S-wave velocities of subsurface structure (Pulliam et al., 2002; Julia et al., 2000, 2005; Mitra et al., 2018). We performed modeling using a joint, non-linear scheme which accounts for the relative influence of each of the datasets during the iterative process of this technique (Agrawal et al., 2015a,b). The joint objective function is defined as follows:

$$JointObjFun = W_{Ps}f\,(C^{Ps}_{data}, C^{Ps}_{syn}) + W_{Sp}f\,(C^{Sp}_{data}, C^{Sp}_{syn}) + W_{Rw}f\,(C^{Rw}_{data}, C^{Rw}_{syn}) \quad (2)$$

where *Ps*, *Sp*, and *Rw* represent Ps and Sp receiver functions and Rayleigh wave group velocity dispersion for real (C_{data}) and synthetic data (C_{syn}), respectively. W_{Ps}, W_{sp}, and W_{Rw} are the relative weights that each dataset will put to influence the joint modeling process. We give equal weights to each of the datasets and used cross-correlation L2-

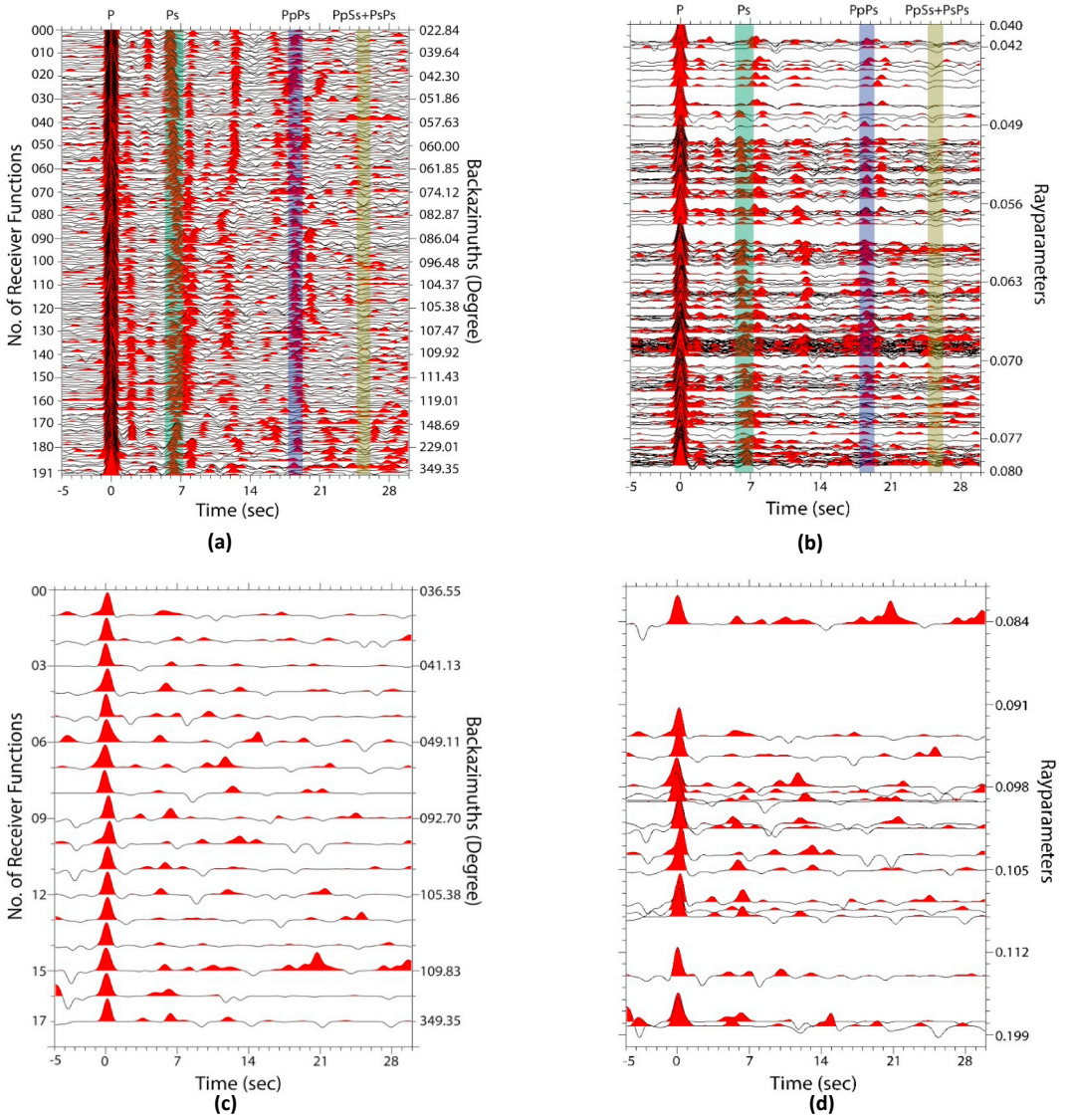

Fig. 4. (a, b) The gather of 191 Ps receiver functions and (c, d) 17 Sp receiver functions, with respect to backazimuths and ray parameters for station ISM. The vertically oriented transparent green, violet and yellow lines represent arrival times of converted phases like Ps, PpPs and PsPs + PpSs, respectively (Fig. 4a and 4b). These arrival times of converted phases are estimated using the results of H-κ stacking. (For interpretation of the references to color in this figure legend, the reader is referred to the web version of this article.)

norm of error function which varies between −1 and 1. The individual error function for each dataset looks like below:

$$f(C_{data}, C_{syn}) = 1 - \frac{2\sum |C^i_{data} - C^i_{syn}|^\alpha}{\sum |C^i_{data} - C^i_{syn}|^\alpha + \sum |C^i_{data} + C^i_{syn}|^\alpha} \quad (3)$$

where parameter 'α' represents the norm.

The joint objective function in Eq. (2) is minimized using a global, non-linear and stochastic optimization technique called as "Very Fast Simulated Annealing (VFSA)", which is a Monte Carlo non-linear optimization method (Sen and Stoffa, 1995; Gangopadhyay et al., 2007; Agrawal et al., 2015a,b). This optimization process is a variant of Simulated Annealing (SA) which was first developed and coded by Kirkpatrick et al. (1983). It is analogous to the physical concept of "Crystal Annealing" (Metropolis et al., 1953; Ingber, 1989). In this concept, a metal in the heat bath is heated to a very high temperature and then allowed to cool down slowly until it reaches and arranged itself in a regular and uniform crystal pattern. During this slow cooling process at each temperature, the metal is provided enough time such that it reaches to an equilibrium stage. Then, the temperature is continued to be lowered with an equilibrium stage to be attained at each temperature such that regular crystal pattern associated with 'minimum energy' can be obtained at final temperature. VFSA begins with Metropolis Monte Carlo simulation accepting each model with some probability (as shown on Eq. (4)), even though the updated error is higher than the previous one, at very high temperature. This probability-dependent acceptance allows this process of optimization to escape a local minimum and continue its broad search of the model space. In SA, the updated models are chosen from Ingber distribution while VFSA prefers its models to be drawn from a Cauchy-like distribution (Sen and Stoffa, 1995). In contrast to Ingber distribution, the Cauchy-like distribution function selects updated models in proximity to the current model at low temperatures and makes it faster than SA. To explain the VFSA technique, a simplified flow-diagram is shown in Fig. 7. The VFSA process begins with an initial model m^i_k with an associated error or energy, $E(m^i_k)$. From a temperature (T) dependent Cauchy-like distribution, $\xi(T)$, it draws a new model or updates the current model (m^i_{k+1}). The error or energy associated with the current model $E(m^i_{k+1})$ is compared with the error or energy associated initial model $E(m^i_k)$ to compute the change in error function (δE). If the change

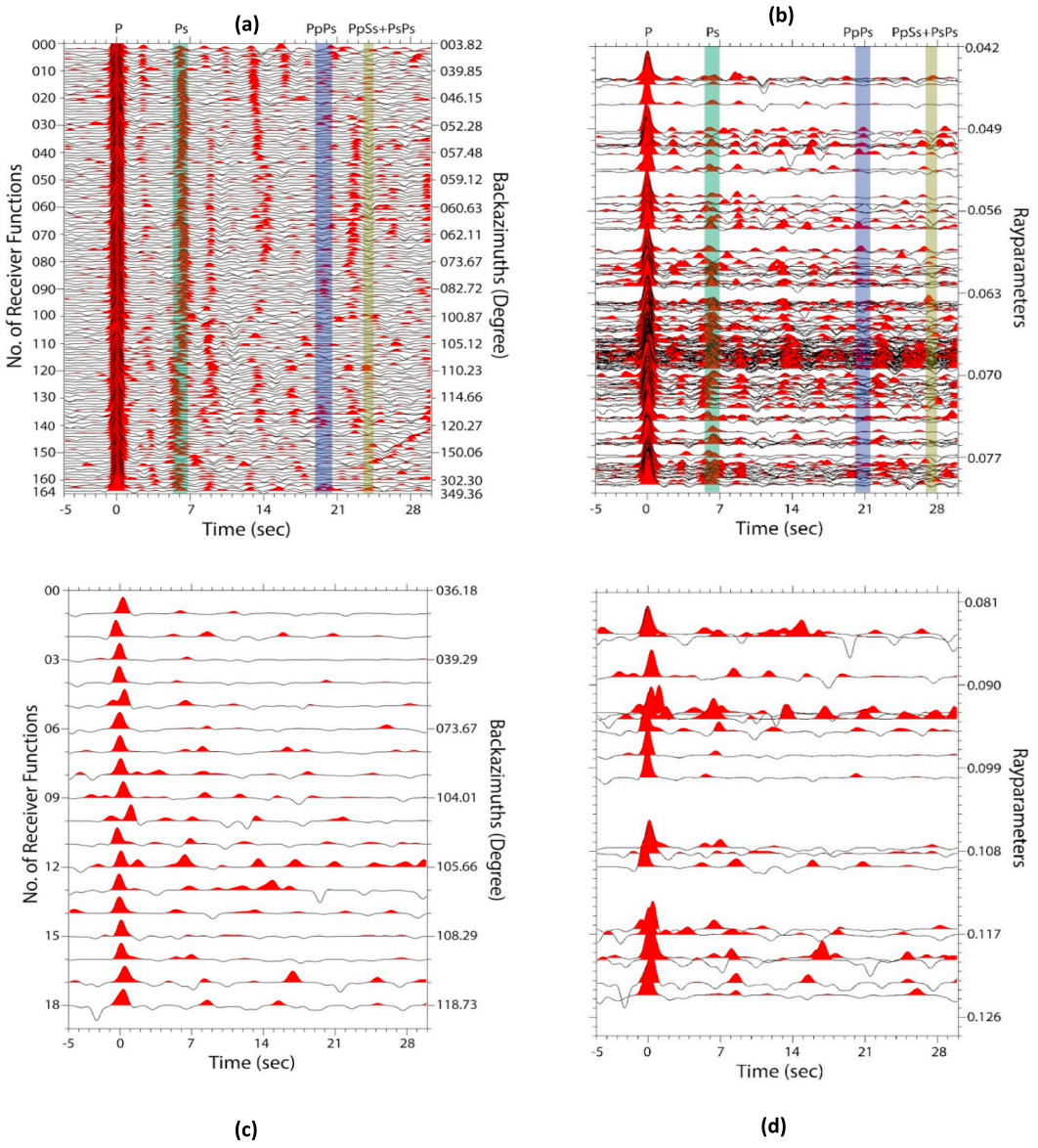

Fig. 5. (a, b) The gather of 164 Ps receiver functions and (c, d) 18 Sp receiver functions, with respect to backazimuths and ray parameters for station BOKR. The vertically oriented transparent green, violet and yellow lines represent arrival times of converted phases like Ps, PpPs and PsPs + PpSs, respectively (Fig. 5a and 5b). These arrival times of converted phases are estimated using the results of H-κ stacking. (For interpretation of the references to color in this figure legend, the reader is referred to the web version of this article.)

in error or energy (δE) is ≤ 0, the new model or updated model is accepted, and replaces the initial model. And if the condition (δE) ≤ 0, is not satisfied, the new model or updated model (m^i_{k+1}) is accepted with a probability of $e^{\frac{\delta E}{T}}$. At each iteration of VFSA, the model is accepted with some probability which is defined by the following criterion:

$$P = \begin{cases} 1, & \delta E < 0 \\ e^{\frac{\delta E}{T}}, & \delta E > 0 \end{cases} \tag{4}$$

where "T" and "δE" represent the temperature and change in energy of the metal at each iteration which is also analogues to the cost (or misfit) function in seismological inverse problems. An update to the current model is generated from the model search space randomly in the following way:

$$m^i_{k+1} = m^i_k + \xi^i (m^i_{max} - m^i_{min}) \tag{5}$$

In the above equation, m^i_{k+1} represents model parameter in "ith" dimension at $(k+1)th$ iteration with m^i_{k+1} belongs to model space $m^i_{k+1} \in [m^i_{min}, m^i_{max}]$. Also, ξ^i is drawn from the Cauchy's like uniform distribution given below:

$$u^i \in [0, 1]$$

$$\xi^i = sgn\left(u^i - \frac{1}{2}\right) T^i \left[\left(1 + \frac{1}{T^i}\right)^{|2u^i - 1|} - 1\right] \tag{6}$$

A slow temperature annealing schedule inversely proportional to iteration number is used by VFSA which is written as follows:

$$T(k) = \frac{T_0}{k} \tag{7}$$

where T_0 and k are initial temperature and iteration number of this joint modeling process via VFSA. This whole procedure is repeated a number of times until the joint objective function converges (Sen and Stoffa, 1995).

For our joint analysis, we prepare the initial 1D Vp and Vs models up to 150 km depth consisting of 18 layers. The Vs model of ISM and

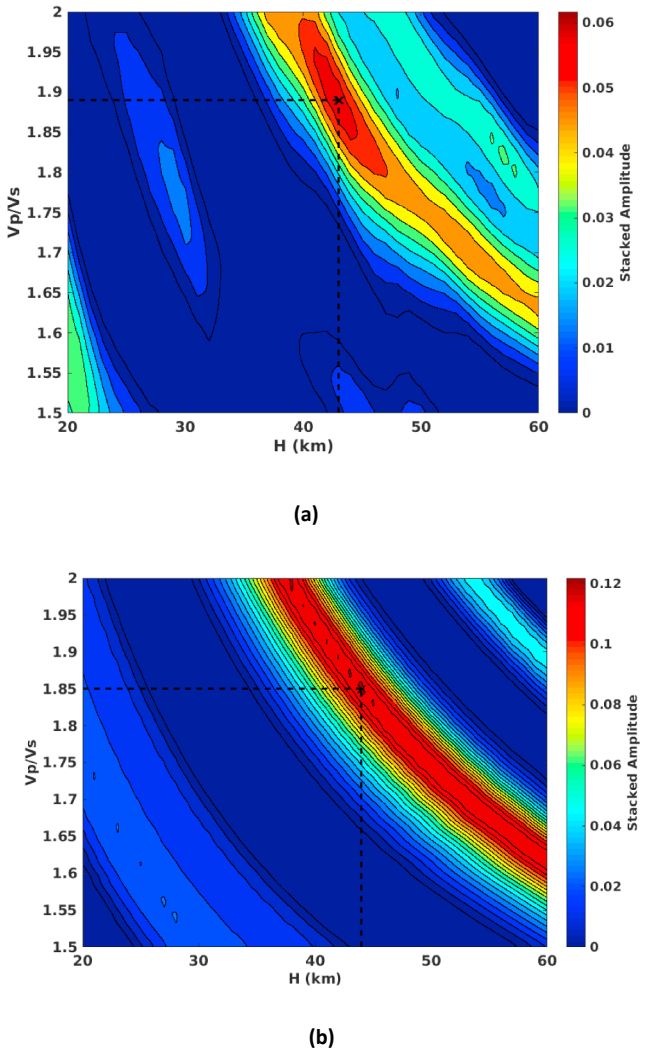

Fig. 6. Results of H-κ stacking for seismic stations ISM and BOKR are shown in Fig. 6a and 6b. The "black color cross" indicates the location of maxima of stacked amplitude where best values of Moho depth (H) and bulk Vp/Vs ratios (κ) are found. The maxima of stacked amplitude of converted phases (i.e. Ps, PpPs and PsPs + PpSs) for seismic station ISM corresponds to Moho depth and bulk Vp/Vs ratio of ~43 km and ~1.89, respectively (Fig. 6a). While for station BOKR, the Moho depth and bulk Vp/Vs ratio are estimated at ~44 km and ~1.85, respectively (Fig. 6b).

BOKR up to Moho depths from previous studies are utilized for the construction of initial models (Mandal and Biswas, 2016; Kosarev et al., 2013). The initial Vp models are prepared by multiplying Vp/Vs ratio (from H-κ stacking) and initial Vs models. The mantle half space Vp and Vs velocities of ak135 are used to form the mantle parts of initial models.

We divided our optimization process into two parts. First, we find the best-fitting model using 3000 iterations. Secondly, we computed uncertainties associated with best-fitting model. We observed, after a set of trials, that the misfit error changes not so much after 2500 iterations, so we set the maximum number of iterations to 3000 to provide a reasonable margin of error (Fig. 8). Our modeling scheme searches for each model parameter (Poisson's Ratio and Vs) within ± 10 percent of starting model. We also performed the trial runs with the model parameters varied within ± 10, ± 15, ± 20 and ± 30 percent of initial values. Our results produced almost similar final models that were within one standard error. Additionally, a significant variation in model parameters is not realistic given the tectonic and geologic setting

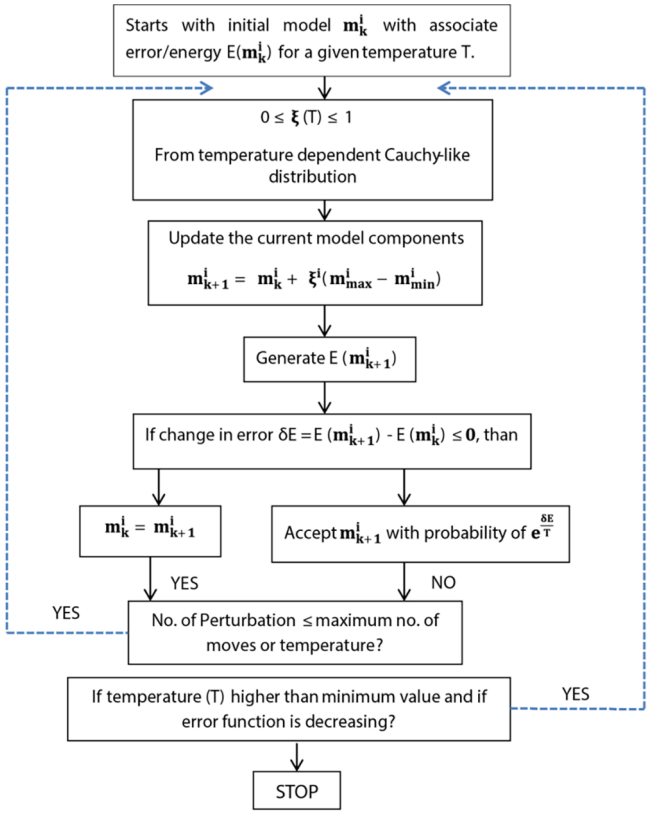

Fig. 7. Basic flow diagram of Very Fast Simulated Annealing (VFSA), global optimization process modified from Gangopadhyay et al. (2007) and Sen and Stoffa (1995). Here, m_k^i represents the initial model with associated energy or error $E(m_k^i)$, while m_{k+1}^i represents the updated model and $E(m_{k+1}^i)$ is the associated error function. T is temperature and $\xi(T)$ represents the temperature dependent Cauchy-like distribution.

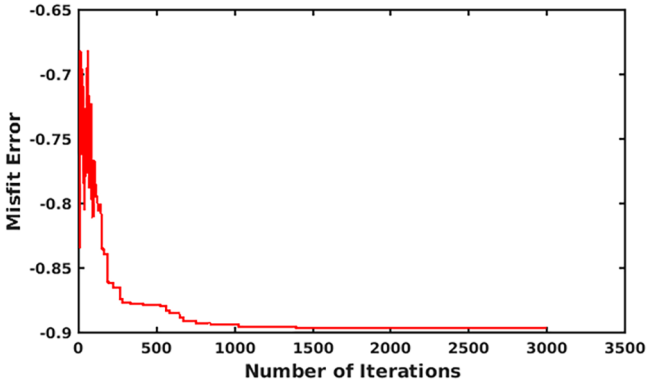

Fig. 8. Plot between number of iterations and misfit error for finding the best fitting model from Very Fast Simulated Annealing (VFSA).

of the regions. Therefore, to maintain reasonable computational time and to allow variations that are more realistic, we vary the model parameters ± 10 percent around the starting velocity model. The uncertainties (i.e. PPDs) are also estimated within −10% to +10% around best-fitting model. For our joint analysis during VFSA run, we set the initial temperature at 10^4 units and allowed it to cool down to 10^{-15} units.

The estimation of uncertainties is an integral and inherent part of this joint analysis method. Hence, for this purpose, we are using Posterior Probability Density functions (PPDs) (Agrawal et al., 2015a). The PPD function is used to distinguish the portions of model parameter search space where acceptable models are more or less probable to

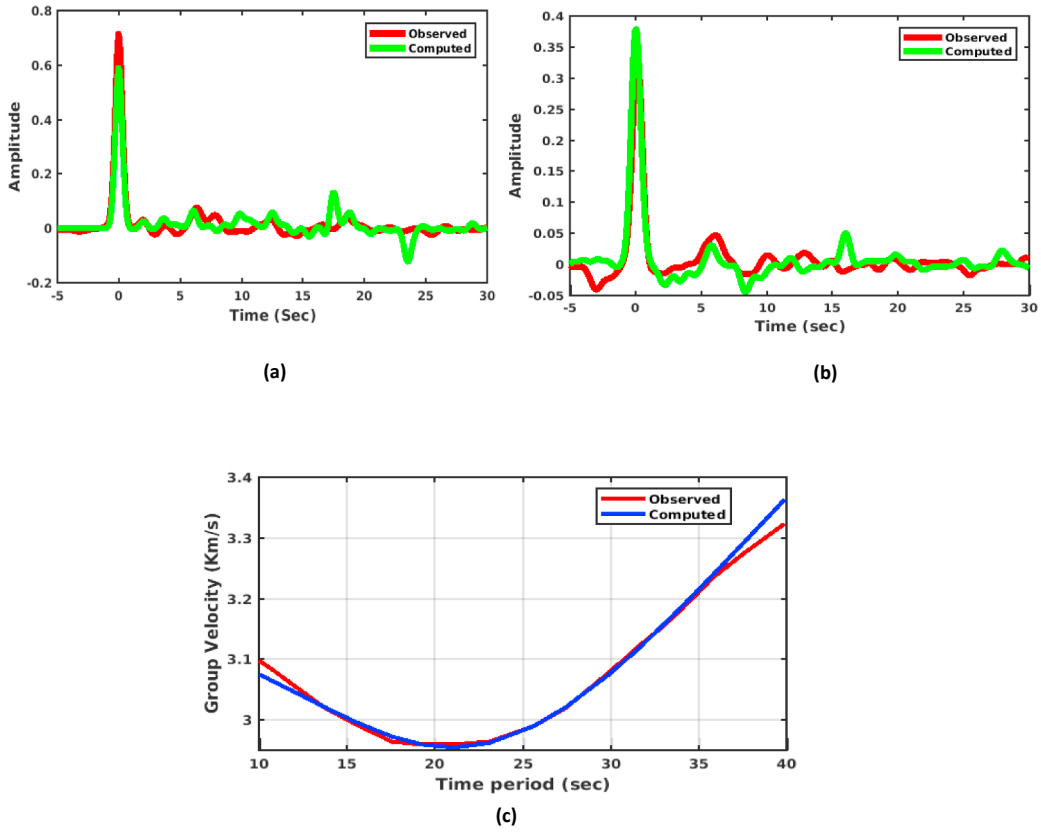

Fig. 9. This figure shows the fits obtained from joint modeling of three datasets for seismic station ISM. (a) Observed (Red) and computed (Green) Ps receiver function (b) Observed (Red) and computed (Green) Sp receiver function and (c) Observed (Red) and computed (Blue) Rayleigh wave group velocity dispersion curve. (For interpretation of the references to color in this figure legend, the reader is referred to the web version of this article.)

occur. A broad or multi-valued misfit function generally suggests that other acceptable solutions of models are either near or far from our best-fitting model (Sen and Stoffa, 1996). The details of this joint modeling technique along with its uncertainty estimation are given in Agrawal et al. (2015a). The PPD function is defined as follows:

$$\sigma(\boldsymbol{m}|\boldsymbol{C_{obs}}) \propto e^{-E(\boldsymbol{m})} p(\boldsymbol{m}) \tag{8}$$

where, $\sigma(\boldsymbol{m}|\boldsymbol{C_{obs}})$ represents the PPD function while $e^{-E(\boldsymbol{m})}$ represents likelihood function. $p(m)$ represents the prior probability of model parameter m, which is independent of data. It describes the information on the model parameter without knowledge of data. It is also called the prior probability distribution function. The prior information can be obtained from observations other than real data (i.e. Ps and Sp receiver functions and dispersion curves) such as outcrops data, the geology of the area etc. The prior probability density function $p(\boldsymbol{m})$ can be defined as follows.

$$p(\boldsymbol{m}) \propto \exp\left[-\frac{1}{2}(\boldsymbol{m} - m^p)^T \boldsymbol{c}_m^{-1}(\boldsymbol{m} - \boldsymbol{m}^p)\right] \tag{9}$$

where $\boldsymbol{m}$ is model parameter, $\boldsymbol{m^p}$ is prior model parameter and c_m is prior model covariance matrix. The prior model covariance matrix can defined as

$$\boldsymbol{c}_m = \int d\boldsymbol{m}(\boldsymbol{m} - \langle m\rangle)(\boldsymbol{m} - \langle m\rangle)^T \sigma(\boldsymbol{m}|\boldsymbol{C_{obs}}) \tag{10}$$

where, $\langle m\rangle$ represents the posterior mean model and it can be define as

$$\langle \boldsymbol{m}\rangle = \int d\boldsymbol{m}\ \boldsymbol{m}\ \sigma(\boldsymbol{m}|\boldsymbol{C_{obs}}) \tag{11}$$

where $\sigma(\boldsymbol{m}|\boldsymbol{C_{obs}})$ represents the PPD function.

This prior information is coupled with likelihood function (or error function) to form the final PPD using model parameter search space (Eq. (8)). The uncertainties estimation (i.e. PPDs) for best fitting models (Vp and Vs) with a search space of −10% to +10% is done by running VFSA multiple times (20 in this study) for both seismic stations (Figs. 12 and 14). The colored region represents the layer-wise search area. The red and yellow colors indicate a higher probability that the accurate velocity will be found at that value. In an ideal case, each layer would have distinct, single-valued and highly peaked distribution. Such a case would infer that the data imposes strong constraints on the model parameters (Figs. 12 and 14).

4. Results and discussion

The lithospheric shear (Vs) and compressional (Vp) wave velocity models are inferred in order to justify our comments on the lithospheric geological processes beneath EPCP by utilizing the large amount of teleseismic earthquake data collected from seismic stations ISM and BOKR (Fig. 3a and b). The 1D seismic Vp and Vs velocity profiles are estimated by jointly imposing the complementary constraints of Ps and Sp receiver functions and Rayleigh wave group velocity dispersion curves; where a three part objective function (Eq. (2)) is optimized via Very Fast Simulated Annealing (VFSA). The steps followed during this joint modeling process are schematically summarized in Fig. 2.

Fig. 4a and b represents the Ps receiver functions' gather plotted with respect to backazimuths and ray parameters for seismic station ISM. While, the Sp receiver functions' gather with respect to back-azimuths and ray parameters for seismic station ISM are shown in Fig. 4c and d, respectively. The Ps receiver functions' gather with respect to backazimuths and ray parameter is shown in Fig. 5a and b, respectively, for seismic station BOKR. Also, the gather of Sp receiver functions has been shown in Fig. 5c and d, respectively, for seismic

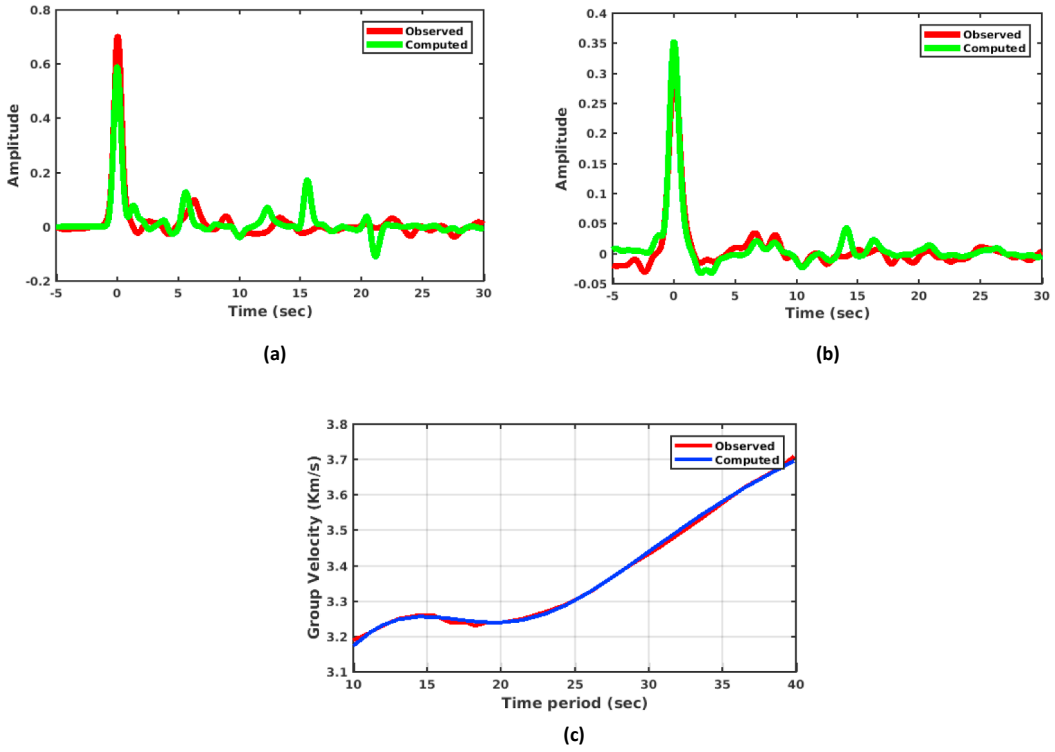

Fig. 10. This figure shows the fits obtained from joint modeling of three datasets for seismic station BOKR. (a) Observed (Red) and computed (Green) Ps receiver function (b) Observed (Red) and computed (Green) Sp receiver function and (c) Observed (Red) and computed (Blue) Rayleigh wave group velocity dispersion curve. (For interpretation of the references to color in this figure legend, the reader is referred to the web version of this article.)

station BOKR. Fig. 6a and b shows the estimates of Moho depths (H) and bulk Vp/Vs ratios (κ) inferred from H-κ stacking of Ps receiver functions for seismic stations ISM and BOKR, respectively. The maxima of stacked amplitude of converted phases (i.e. Ps, PpPs and PsPs + PpSs) for seismic station ISM correspond to Moho depth and bulk Vp/Vs ratio of ~43 km and ~1.89, respectively (Fig. 6a). While for station BOKR, the Moho depth (H) and bulk Vp/Vs (κ) ratio are estimated at ~44 km and ~1.85, respectively (Fig. 6b). Our Moho depth estimates for station ISM and BOKR are in good agreement with earlier studies (Bhattacharya and Shalivahan, 2002; Kayal et al., 2011; Kosarev et al., 2013; Sharma et al., 2014; Mandal and Biswas, 2016).

Bhattacharya and Shalivahan (2002) speculated a greater crustal

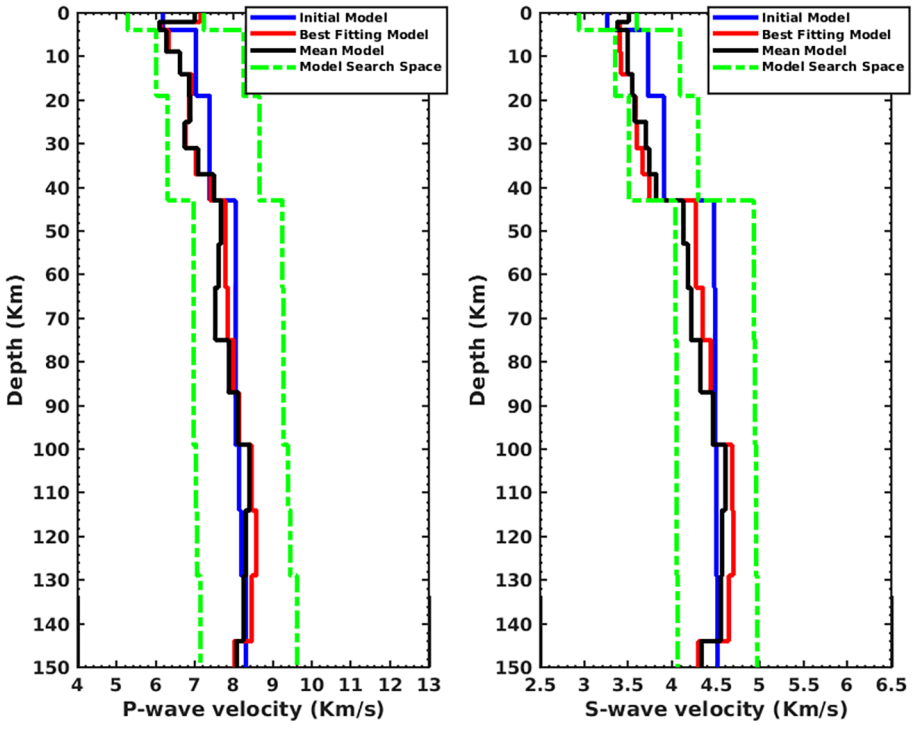

Fig. 11. Represent Vp and Vs models of crustal and uppermost mantle structure for seismic stations ISM using three datasets namely Ps, Sp receiver functions and Rayleigh wave group velocity dispersion curve. The starting models is shown in solid blue color where the crustal shear wave velocities are obtained from the previous study of Nirsa area (Mandal and Biswas, 2016). The upper mantle Vs velocities in the starting model are same as ak135. The solid red line represents the best-fitting model found from joint inversion with search space of ± 10% (dashed green lines) around the initial model. The solid black line represents the mean model obtained from 20 VFSA runs for the estimation of PPDs. (For interpretation of the references to color in this figure legend, the reader is referred to the web version of this article.)

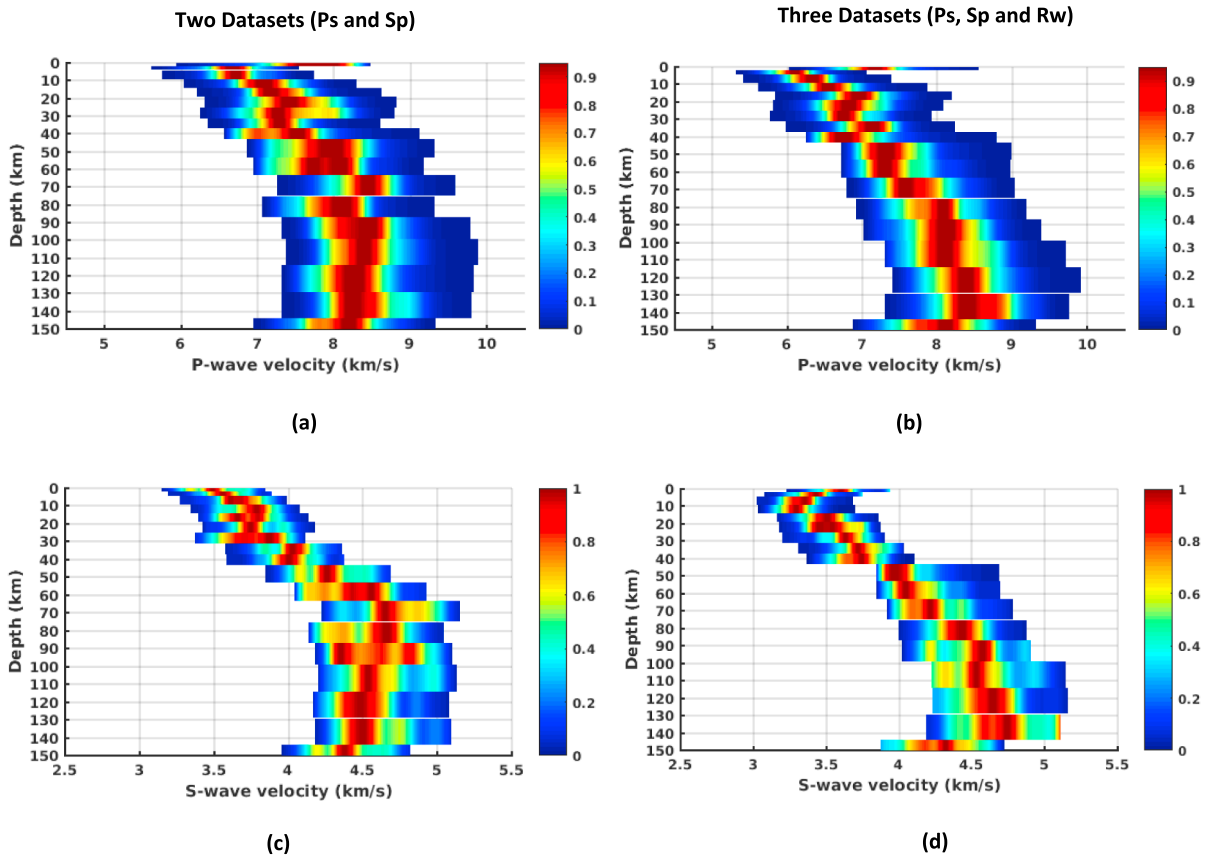

Fig. 12. Represent comparison between Posterior Probability Density (PPDs) plot of two and three datasets for seismic station ISM. PPDs are plotted around best-fitting models with search space of ± 10%. (a) Plot of Vp PPD using two datasets (Ps and Sp receiver functions) (b) Plot of Vp PPD using three datasets (Ps, Sp receiver functions and Rayleigh wave group velocity dispersion curve) (c) Plot of Vs PPD using two datasets (d) Plot of Vs PPD using three datasets.

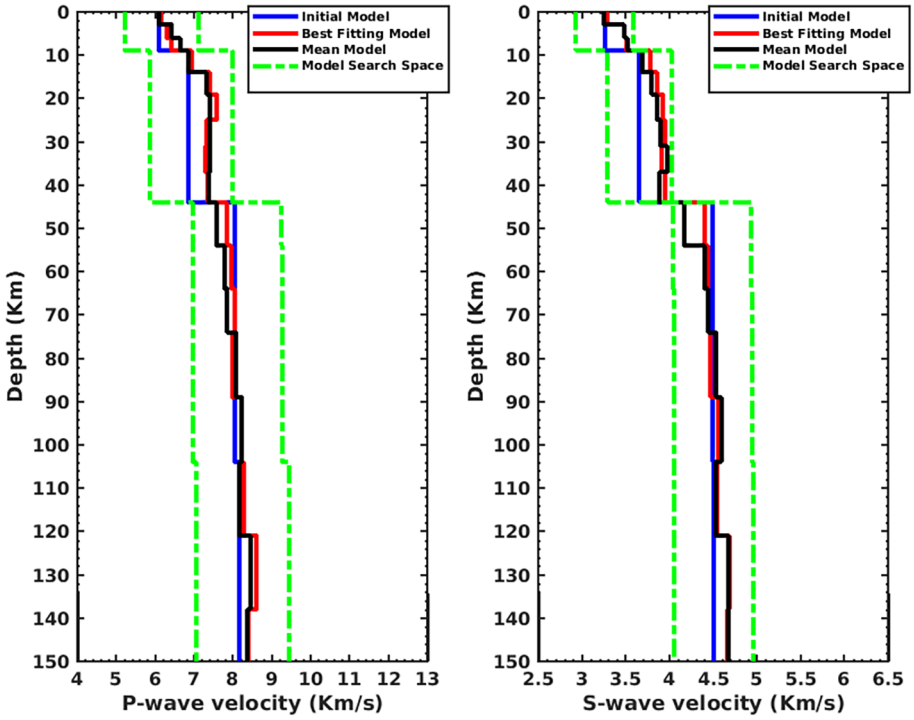

Fig. 13. It represents Vp and Vs models of crustal and uppermost mantle structure for seismic stations BOKR, using three datasets namely Ps, Sp receiver functions and Rayleigh wave group velocity dispersion curve. The starting model is shown in solid blue color where the crustal shear wave velocities are obtained from the previous study (Kosarev et al., 2013) for seismic station BOKR. The upper mantle Vs velocities are same as ak135. The solid red line represents the best-fitting model obtained from VFSA with search space of ± 10% (dashed green lines) around the starting model. The solid black line represents the mean of all the acceptable models. (For interpretation of the references to color in this figure legend, the reader is referred to the web version of this article.)

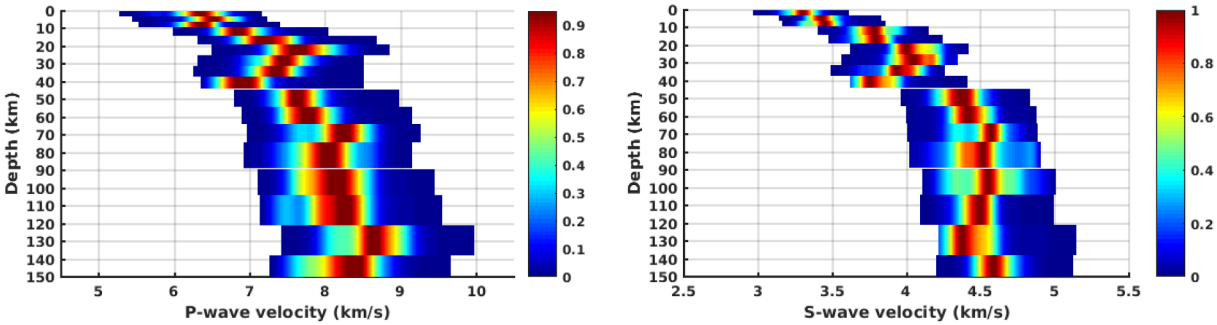

Fig. 14. Plot of Posterior Probability Density (PPDs) functions using three datasets (Ps and Sp receiver functions and Rayleigh wave group velocity dispersion curve). PPDs are estimated around best-fitting models with search space of ± 10% for station BOKR, (a) Plot of Vp PPD and, (b) Plot of Vs PPD.

thickness i.e., 46 km ± 2.1 km beneath the East Indian Craton (EIC) from magnetotelluric survey. They find the upper mantle resistivity of EIC is significantly low ~750 ohm-m in comparison to the lower crust of about ~8500 ohm-m. Thereafter, Kayal et al. (2011) performed linearized inversion of Ps receiver functions using 17 teleseismic events to develop the subsurface 1D shear wave velocity model beneath seismic station ISM. They reported that the crust-mantle boundary (i.e. Moho) may lie at a depth of ~41 km for the same seismic station. Sharma et al. (2014) found that the Moho depth and bulk Vp/Vs ratio for the same station lies at ~42.2 km and ~1.92, respectively. Their estimates are in close resemblance to our Moho depth and bulk Vp/Vs ratio obtained from H-κ stacking performed for seismic station ISM. Also, the technique of differential evolution waveform inversion of receiver functions was applied in the region of Nirsa, which is in close proximity (nearly 40 km) of seismic station ISM. They deduced that the Moho is located at a depth of ~41.4 km (Mandal and Biswas, 2016) which is also comparable to our results from H-κ stacking (Fig. 6a). Prior to this, sequential modeling of Ps and Sp receiver functions was carried out by Kosarev et al. (2013) using linearized optimization process. They estimate the Moho depth of ~45 km beneath Bokaro (Fig. 6b). During our H-κ stacking process, the converted phases Ps, PpPs and PsPs + PpSs for seismic stations ISM and BOKR are observed to be arriving at ~6.36 s, 18.81 s, 25.18 s and 6.25 s, 18.89 s, 25.18 s respectively (Figs. 4(a, b) and 5(a-b)).

Figs. 9 and 10 show the fits obtained from joint modeling of three datasets namely, Ps receiver functions, Sp receiver functions and Rayleigh wave group velocity dispersion curves for seismic station ISM and BOKR, respectively. The observed and computed Ps and Sp receiver functions are represented in red and green colors, respectively. While, the observed and computed Rayleigh wave group velocity dispersion curves are shown in red and blue colors. For seismic station ISM and BOKR, the 1D compressional (Vp) and shear (Vs) waves velocity profiles obtained from joint analysis of Ps, Sp receiver functions and Rayleigh wave group velocity dispersion curves via nonlinear optimization process of VFSA are shown in Figs. 11 and 13. The dashed green lines represent the model search space with −10% to +10% around the initial model for finding the best-fitting model. The black lines show the mean of all the acceptable Vp and Vs models which fit Ps, Sp receiver functions and Rayleigh wave group velocity dispersion curves quite reasonably (i.e. more than 89%). The best-fitting models (Vp and Vs) are represented in solid red lines for seismic stations ISM and BOKR (Figs. 11 and 13). In best fitting model for station ISM, the Vs varies between 3.3 km/s to 4.8 km/s, and Vp varies between 6.1 km/s and 8.4 km/s from surface to the depth of ~150 km. At ~43 km depth, the value of Vp and Vs increase significantly and abruptly from ~7.3 km/s to ~7.8 km/s and ~3.7 km to ~4.2 km/s; which indicates the location of Moho (Fig. 11). We observe that Vp and Vs ranges between ~6.2 km/s to ~8.3 km/s and ~3.2 km/s to ~4.6 km/s, respectively, for seismic station BOKR. At the location of Moho i.e. ~44 km depth for BOKR, the value of Vp and Vs increase substantially and suddenly from ~7.3 km/s to ~7.8 km/s and ~4.0 km to ~4.4 km/s (Fig. 13). These depths of crustal-mantle boundary in EPCP are comparatively higher than the central part of the country which may be due to the downwarping of the mantle (Suresh et al., 2014). Previous studies have also confirmed these relatively high shear and compressional wave velocities under the Proterozoic and Archean formation of the Indian Shield (Kumar et al., 2001).

The higher value of Poisson's ratio (> 0.25) is interpreted as intermediate to mafic composition, the composition of crust particularly in Precambrian cratons are mainly felsic-to-intermediate and mafic for the lower crust (Zandt and Ammon, 1995). Our calculated Poisson's ratio for station ISM and BOKR are 0.30 and 0.29, respectively (From Eq. (1)). These higher values of more than global average Poisson's ratios are in good agreement with Zandt and Ammon (1995), and indicate towards the presence of mafic rocks with partial melts in the lower crust. Rao and Rao (1983) deduced that the average heat flow for the Damodar valley in the range of 69–79 mW/m^2. They also conducted temperature measurements through borehole study in Bokaro and established that the heat flow of ~73 mW/m^2 is present in the region (Rao and Rao, 1983). This heat flow value for Bokaro is above than average continental heat flow value (i.e. ~65 mW/m^2) which may further confirms that there is a possibility of mafic rocks with partial melts in the lower crust of EPCP. Previous studies have indicated that various mafic dike swarms are present on the surface of EPCP which suggest the crust in this area was under plated by mafic cumulates (Murthy, 1987).

To verify the reliability of velocity profiles, estimation of uncertainties must be an inherent and integral part of any modeling technique. We calculate these uncertainties using Posterior Probability Density (PPD) functions. These PPDs guide us toward the types and characteristics of additional data that should be sought in order to improve model constraints and, therefore, model reliability. Additionally, this tool help us in quantitatively determining the sections of the best fitting model which are well or less constrained. We estimate Vp PPDs and Vs PPDs within ± 10% search space of their corresponding best fitting models (Figs. 11 and 13). To have the confidence in the Vp and Vs models described earlier, a confirmatory test is also conducted for seismic station ISM. This test basically explains how modeling three datasets (i.e. Ps and Sp receiver functions and Rayleigh wave group velocity dispersion curve) may provide comparatively well constrained, more unique velocity profiles than modeling only two datasets (i.e. Ps and Sp receiver functions). During this test, an additional modeling using only two, i.e. Ps and Sp receiver functions, is also performed to compare its outcomes with the modeling results of three datasets together. The best-fitting models of Vp and Vs profiles for seismic station ISM are computed using two and all datasets simultaneously. Then, PPDs are generated with model search space of ± 10% around these best fitting Vp and Vs models ((Fig. 12(a–d)). It is to be noted that the broad and highly peaked PPD values (i.e. Red and yellow colors) may represent a high level of uncertainty with more number of

acceptable models in comparison to where a narrow and highly peaked PPD will be observed. The narrower peaks represent more unique and highly constrained best-fitting model. It is observed that the best-fitting model obtained using three datasets is more unique and generally well constrained than the model computed from two datasets. For example, the Vp PPD plot of two datasets shows mostly broad and multiple peaks at the depth of ~40 km and ~60 km from the surface, which indicates towards more uncertainties and less reliable best-fitting model for these layers; while Vp PPD plot of three datasets shows mostly narrower single red peak without multiples for the same layers, which represents relatively less uncertainties and more reliable best-fitting model (Fig. 12a and b). Overall, Vp PPDs for three datasets contains generally narrower, distinct and highly peaks PPDs relative to two datasets. Likewise, Vs PPD in the case of two datasets are broad having multiple peaked high probability regions (layers at ~30 km, ~60 km, ~80 km, ~90 km and ~120 km) in comparison to three datasets (Fig. 12c and d). These evidences confirms that jointly modeling three datasets produces well constrained, more unique and more reliable solution for velocity profiles in comparison to two datasets. Likewise, PPDs for Vp and Vs are also estimated for seismic station BOKR where Vp PPD shows that all layers contain single, distinct and peaked high probability red color region which indicates that almost all layers (except layers at the depths of ~100 km and ~110 km from the surface) have been identified with smaller uncertainties (Fig. 14a). Similarly, Vs PPD shows that all layers are comparatively narrowly peaked associated with higher constraints and more unique (except layers at the depths of ~30 km, ~80 km and ~130 km from the surface) (Fig. 14b).

5. Conclusions

We use joint modeling technique to infer the crustal thickness, shear and compressional wave velocity structure of the eastern part of Chhotanagpur Plateau (EPCP) of Stable Continental Peninsular Region (SCPR). The complementary constraints of dissimilar datasets such as Ps, Sp receiver functions and Rayleigh wave group velocity dispersion curves are used to obtain best fitting Vp and Vs models via Very Fast Simulated Annealing (VFSA). We use high quality teleseismic earthquakes' waveforms ($5.5 \leq M \leq 8.0$) recorded at two seismic stations ISM and BOKR located in Dhanbad and Bokaro, respectively. We divided our optimization procedure in two parts to find the best fitting models and associated uncertainties in terms of Posterior Probability Density (PPD) functions. Our results indicate that on an average the eastern part of Chhotanagpur plateau which is mostly composed of Granite Gneiss Complex with high heat flow is characterized by the thick crust. We observe that Poisson's ratios of 0.30 and 0.29 for ISM and BOKR which are larger than global average (i.e. > 0.25). These higher values of Poisson's ratios may indicate the presence of mafic rocks and partial melts in lower crust of EPCP. For ISM station, Vp and Vs vary between 3.3 km/s–4.8 km/s and 6.1 km/s–8.4 km/s, respectively, from surface to the depth of ~150 km. We observe that Vp and Vs ranges between ~6.2 km/s to ~8.3 km/s and ~3.2 km/s to ~4.6 km/s, respectively, for seismic station BOKR. Our results reveal that the crust is relatively thicker than the central part of the Indian Shield which may be due to down-warping of the mantle. A confirmatory test is also performed where PPDs computed from modeling of two datasets (i.e. Ps and Sp receiver functions) and three datasets (i.e. Ps and Sp receiver functions and Rayleigh wave group velocity dispersion curves) are compared. This test proves that PPDs from all datasets generally show single, distinct and peaked high probability region in contrast to two datasets where relatively broad, multiple peaked PPDs are observed. It confirms that jointly modeling three datasets produces well constrained, more unique and more reliable solution for velocity profiles in comparison to two datasets.

Acknowledgements

The data used in this study for Bokaro seismic station were obtained from Indian Meteorological Department (IMD), New Delhi. We thank Prof. R.B. Herrmann and I.W. Bailey for making their codes freely available which helped us in computation of dispersion curves and receiver functions. We also thank Prof. Mrinal K. Sen and Prof. Jay Pulliam for helping us in estimation of uncertainties using statistical tool. The authors are also thankful to Shri Raj Kumar Prasad for providing earthquake data recorded at the ISM broadband station. Mr. Anupam Patel is also appreciated for helping the lead author in modifying some figures of this paper. The authors are greatly thankful to the editor Vernon Cormier and two anonymous reviewers for their constructive comments which eventually helped in improving the quality of this manuscript. This research was supported by funding from the Department of Science and Technology (SERB Project Number: ECR/2016/001271), Govt. of India and Faculty Research Scheme grant (Project No. FRS (103)/2016-2017/AGP) provided by Indian Institute of Technology (Indian School of Mines), Dhanbad.

Appendix A. Supplementary data

Supplementary data to this article can be found online at https://doi.org/10.1016/j.pepi.2019.01.004.

References

Agrawal, M., Pulliam, J., Sen, M.K., Dutta, U., Pasyanos, M., Mellors, R., 2015a. Crustal and uppermost mantle structure in the Middle East: assessing constraints provided by jointly modeling Ps and Sp receiver functions and Rayleigh wave group velocity dispersion curves. Geophys. J. Int. 201 (2), 783–810. https://doi.org/10.1002/2015GC005803.

Agrawal, M., Pulliam, J., Sen, M.K., Gurrola, H., 2015b. Lithospheric structure of the Texas-Gulf of Mexico passive margin from surface wave dispersion and migrated Ps receiver functions. Geochem. Geophys. Geosyst. 16, 2221–2239. https://doi.org/10.1002/2015GC005803.

Ammon, C.J., Randall, G.E., Zandt, G., 1990. On the non-uniqueness of receiver function inversions. J. Geophys. Res. 95, 15303–15318.

Bhattacharya, S.N., 1971. Seismic surface-wave dispersion and crust-mantle structure of the Indian Peninsula. Indian J. Meteorol. Geophys. 22, 179–186.

Bhattacharya, B.B., Shalivahan, 2002. The electric moho underneath Eastern Indian Craton. Geophys. Res. Lett. 29. https://doi.org/10.1029/2001GL014062.

Dziewonski, A., Bloch, S., Landisman, M., 1969. Surface wave ray tracing azimuthal anisotropy: a generalized spherical harmonic approach technique for the analysis of transient seismic signals. Bull. Seismol. Soc. Am. 59, 427–444.

Gangopadhyay, A., Pulliam, J., Sen, M.K., 2007. Waveform modeling of teleseismic S, SP, SsPmP, and shear-coupled PL waves for crust and upper mantle velocity structure beneath Africa. Geophys. J. Int. 170, 1210–1226.

Ghose, N.C., Chatterjee, N., Mukherjee, D., Kent, R.W., Saunders, A.D., 2008. Mineralogy and geochemistry of the Bengal Anorthosite massif in the Chotanagpur Gneissic Complex at the eastern Indian shield margin. J. Geol. Soc. India 72, 263–277.

Herrmann, R.B., 1973. Some aspects of band-pass filtering of surface waves. Bull. Seismol. Soc. Am. 63, 663–671.

Ingber, L., 1989. Very fast simulated reannealing. Math. Comput. Model. 12, 967–993.

Julia, J., Ammon, C.J., Herrmann, R.B., Correig, A.M., 2000. Joint inversions of receiver function and surface wave dispersion observations. Geophys. J. Int. 143, 99–112.

Julia, J., Ammon, C.J., Nyblade, A.A., 2005. Evidence for mafic lower crust in Tanzania, East Africa, from joint inversion of receiver functions and Rayleigh wave dispersion velocities. Geophys. J. Int. 162, 555–569.

Kayal, J.R., Srivastava, V.K., Kumar, P., Chatterjee, R., Khan, P.K., 2011. Evaluation of crustal and upper mantle structures using receiver function analysis: ISM broadband observatory data. J. Geol. Soc. India 78, 76–80.

Kirkpatrick, S., Gelatt, C.D., Vecch, M.P., 1983. In: Optimization by Simulated Annealing. Vol. 220, Science, New Series, pp. 671–680.

Kosarev, G.L., Oreshin, S.I., Vinnik, L.P., Kiselev, S.G., Dattatrayam, R.S., Suresh, G., Baidya, P.R., 2013. Heterogeneous lithosphere and the underlying mantle of the Indian subcontinent. Tectonophysics 592, 175–186.

Kumar, M.R., Saul, J., Sarkar, D., Kind, R., Shukla, A., 2001. Crustal structure of the Indian shield; new constraints from teleseismic receiver functions. Geophys. Res. Lett. 28, 1339–1342.

Kumar, P., Yuan, X., Kind, R., Kosarev, G., 2005. The lithosphere asthenosphere boundary in the Tien Shan-Karakoram region from S receiver functions: evidence for continental subduction. Geophys. Res. Lett. 32 (2005), L07305. https://doi.org/10.1029/2004GL022291.

Kumar, S., Agrawal, M., 2018. Joint modeling of receiver functions and dispersion curves for southern Indian Shield. J. Arab. Geosci.

Langston, C.A., 1979. Structure under Mount Rainier, Washington, inferred from

teleseismic body waves. J. Geophys, Res. 84 (4), 749–762.
Ligorria, J.P., Ammon, C., 1999. Iterative deconvolution and receiver function estimation. Bull. Seismol. Soc. Am. 89, 1395–1400.
Mahadevan, T.M., 2002. Geology of Bihar & Jharkahnd. Geol. Soc., India, Bangalore, pp. 563.
Mandal, P., Biswas, K., 2016. Teleseismic receiver functions modeling of the eastern Indian craton. Phys. Earth Planet. Inter. 258, 1–14.
Meert, J.G., Pandit, M.K., Pradhan, V.R., Banks, J., Sirianni, R., Stroud, M., Newstead, B., Gifford, J., 2010. Precambrian crustal evolution of Peninsular India: A 3.0 billion year odyssey. J. Asian Earth Sci. 39, 483–515.
Metropolis, N., Rosenbluth, A.W., Rosenbluth, M.N., Teller, A.H., Teller, E., 1953. Equation of state calculations by fast computing machines. J. Chem. Phys. 21, 1087–1092.
Mitra, S., Priestley, K.F., Borah, K., Gaur, V.K., 2018. Crustal structure and evolution of the Eastern Himalayan plate boundary system, Northeast India. J. Geophys. Res. 123. https://doi.org/10.1002/2017JB014714.
Mukhopadhyay, J., Beukes, J.N.J., Armstrong, R.A., Zimmermann, U., Ghosh, G., Medda, R.A., 2008. Dating the oldest greenstone in India: A 3.51-Ga precise U-Pb SHRIMP zircon age for dacitic lava of the southern iron ore group, Singhbhum Craton. J. Geol. 116 (5), 449–461.
Murthy, N.G.K., 1987. Mafic dyke swarms of the Indian shield, in Mafic Dyke Swarms, edited by H. C. Halls and W. F. Fahrig. Geol. Assoc. Can. Spec. Pap. 34, 393–400.
Naqvi, S.M., Rogers, J.J.W., 1987. Precambrian Geology of India. Oxford University Press, Oxford.
Owens, T.J., Zandt, G., Taylor, S.R., 1984. Seismic evidence for an ancient rift beneath the Cumberland plateau, Tennessee: a detailed analysis of broadband teleseismic P waveforms. J. Geophys. Res. 89. https://doi.org/10.1029/JB089iB09p07783.
Ozalaybey, S., Savage, M.K., Sheehan, A.F., Louie, J.N., Brune, J.N., 1997. Shear-wave velocity structure in the northern Basin and Range province from the combined analysis of receiver functions and surface waves. Bull. Seismol. Soc. Am. 87, 183–199.
Pulliam, J., Sen, M.K., Frohlich, C., Grand, S., 2002. Waveform modelling of the crust and upper mantle using S, Sp, SsPmP and shear-coupled PL waves. In: Proceedings of the 24th Seismic Research Review—Nuclear Explosion Monitoring: Innovation and Integration, pp. 144–153.
Qureshy, M.N., 1971. Relation of gravity to elevation and rejuvenation of block in India. J. Geophys. Res. 76, 545–557.
Rao, G.V., Rao, R.U.M., 1983. Heat flow in the Indian Gondwana basins and heat production of their basement rocks. Tectonophysics 91, 105–117.
Ratheesh Kumar, R.T., Windley, B.F., Rajesh, V.J., Santosh, M., 2013. Elastic thickness structure of the Andaman subduction zone: implications for convergence of the Ninetyeast Ridge. J. Asian Earth Sci. 78, 291–300.
Sen, M.K., Stoffa, P.L., 1995. Global Optimization Methods in Geophysical inversion. Elsevier Science Publishing Company, pp. 281.
Sen, M.K., Stoffa, P.L., 1996. Bayesian inference, Gibbs' sampler and uncertainty estimation in geophysical inversion. Geophys. Prospect. 44, 313–350.
Singh, S.P., 1997. Geochemistry of acid volcanics of the Dalma Group, Singhbhum, Eastern India. J. Geol. Soc. India 49, 437–441.
Sharma, N.K., Khan, P.K., Bhukta, K.K., 2014. Nature of the Moho in the mid-eastern part of the Chotanagpur Plateau, India, from a receiver function perspective. J. Arab. Geosci. https://doi.org/10.1007/s12517-014-1648-8.
Suresh, G., Teotia, S.S., Bhattacharya, S.N., 2014. Crustal velocity structure of the Deccan Volcanic Province, Indian Peninsula, from observed surface wave dispersion. Ann. Geophys. 57 (4), S0431. https://doi.org/10.4401/ag-6540.
Tanimoto, T., 1991. Waveform inversion for three-dimensional density and S-wave structure. J. Geophys. Res. 96, 8167–8189.
Zandt, G., Ammon, C.J., 1995. Continental crust composition constrained by measurements of crustal Poisson's ratio. Nature 374 (6518), 152–154.
Zhu, L., Kanamori, H., 2000. Moho depth variation in southern California from teleseismic receiver functions. J. Geophys. Res. 105, 2969–2980.